ACS APPLIED MATERIALS & INTERFACES

Research Article

www.acsami.org

Controllable Low Temperature Vapor-Solid Growth and Hexagonal Disk Enhanced Field Emission Property of ZnO Nanorod Arrays and Hexagonal Nanodisk Networks

Fan Yang,[†] Wei-Hua Liu,[‡] Xue-Wen Wang,[†] Jie Zheng,[‡] Ru-Yu Shi,[†] Hua Zhao,[†] and He-Qing Yang*[,†]

[†]Key Laboratory of Macromolecular Science of Shaanxi Province, School of Materials Science and Engineering, Shaanxi Normal University, Xi'an, 710062, China

[‡]School of Electronic and Information Engineering, Xi'an Jiaotong University, Xi'an, 710049, China

ABSTRACT: ZnO nanorod arrays and nanodisk networks were grown directly on Si substrate by thermal evaporation of $ZnCl_2$ powder and a mixture of $ZnCl_2$ and $InCl_3{\cdot}4H_2O$ at 450 °C in air, respectively. The ZnO nanorods with the diameters of 0.64 to 0.91 μm and length of about 5.1 μm are single crystalline with the hexagonal structure and grow along the [001] direction. The nanodisk has perfect hexagonal shape, grow mainly along the $\langle 01\bar{1}0 \rangle$ directions, and are enclosed by $\pm(0001)$ top and bottom surfaces. ZnO nanoparticle films oriented in the [001] direction formed first served as seeds, and grow into nanorod arrays via the vapor-solid (VS) process. However, when $InCl_3{\cdot}4H_2O$ was introduced into the reaction system ZnO thick nanosheet films are first formed because of the local segregation of the doping element of indium. The ZnO thick nanosheet films served as seeds, and grow into nanodisk networks via the V−S process. Photoluminescence and field emission properties of the as-obtained ZnO nanorod arrays and hexagonal nanodisk networks have been studied. It was found that the hexagonal nanodisk networks exhibit strong blue-green emissions originated from defect states and enhanced field emission property.

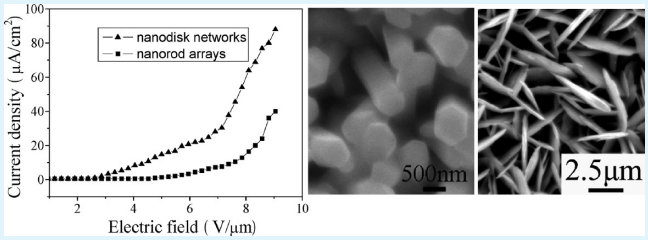

KEYWORDS: *ZnO nanorod arrays, ZnO nanodisk networks, vapor-solid growth, field emission property*

1. INTRODUCTION

It is well-known that the physical and chemical properties of nanomaterials are strongly related to their size and morphology, and then, synthesis of size- and morphology-controlled nanostructures is important in controlling their physical and chemical properties. ZnO is an important semiconducting material with a direct wide band gap (3.37 eV) and large exciton binding energy (60 meV).[1] It has been considered as a perspective material for lasers, light emitting diodes, photodetectors, chemical sensors, solar cells, and photocatalysis owing to its excellent optical and electrical properties.[2] Since the discovery of ZnO nanobelts in 2001,[3] research into ZnO nanomaterials with well-defined sizes and geometric morphology has rapidly developed. Up to now, various synthetic methods such as thermal evaporation, chemical vapor deposition (CVD), pulsed laser deposition, hydrothermal/solvothermal route and colloid chemistry method have been developed for the fabrication of ZnO nanostructures in various geometrical morphologies, including ZnO nanorods,[4] -tubes,[5] -needles,[6] -belts,[3] -nails,[7] -rings,[8] -bows,[9] -springs,[10] -helices,[11] -disks,[12] -combs,[13] -cages,[14] -tetrapods,[15] hexagonal nanocones,[16] star-shaped structures,[17] branched hierarchical structures,[18] nanowire networks,[19] nanowire arrays,[20] nanorod arrays,[21] and nanopropeller arrays.[22] ZnO nanowires, nanobelts and nanorod arrays have been used to fabricate nanoscale light emitting diodes,[23] lasers,[24] dye-sensitized solar cells,[25,26] field-effect transistors,[27] nanogenerators,[28,29] gas sensors,[30,31] and logic circuits.[32]

On the other hand, high-quality field emitters are very desirable for application in wide ranges of field emission-based devices such as flat-panel displays, parallel-electron-beam microscopes, vacuum microwave amplifiers, etc.[33] Among all inorganic materials, only ZnO can be prepared in a variety of sizes, shapes, and aspect ratios. This material can display excellent field emission (FE) properties.[34] The FE property of nanorod/nanowire arrays,[35−39] tetrapods,[40] nanocone arrays,[41] nanoneedles,[42] and hierarchical nanostructures constructed with nanowires[43] of ZnO has been investigated. However, the investigation on FE property of two-dimensional ZnO nanostructures is quite rare.[44,45] To our knowledge, FE properties of the ZnO hexagonal nanodisk networks have not been reported until now although nanostructures with a sharp tip are considered to be a good candidate for FE.[46] In addition, vapor transport and condensation methods for the ZnO nanostructures usually require high temperature (800−1400 °C).[3,12,21]

Based on the synthesis of In-doped ZnO nanometer disks[47] and volatility of the chlorides, we develop a very simple,

Received: March 31, 2012
Accepted: June 25, 2012
Published: June 25, 2012

environmental friendly and low temperature vapor-solid growth route (450 °C) for the large-scale controllable fabrication of ZnO nanorod arrays and hexagonal nanodisk networks. The ZnO nanorod arrays were directly grown on a single crystalline Si substrate by heating anhydrous zinc chloride ($ZnCl_2$) at 450 °C in air. ZnO hexagonal nanodisk networks are obtained by introducing $InCl_3{\cdot}4H_2O$ in the raw material. Field emission properties of the two kinds of ZnO nanostructures have been studied. The as-synthesized ZnO nanodisk networks exhibit enhanced FE properties in comparison with ZnO nanorod arrays.

2. EXPERIMENTAL SECTION

Synthesis of ZnO nanorod arrays and hexagonal nanodisk networks was carried out in a conventional muffle furnace. The experimental setup is shown in Figure 1. **ZnO nanorod arrays:** In a concrete

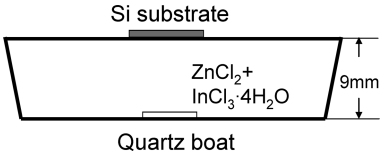

Figure 1. Schematic of the experimental setup for the fabrication of ZnO nanorod arrays and nanodisk networks.

experiment, 0.040 g of $ZnCl_2$ powders was put into a quartz boat. A (111) silicon substrate (p-type with resistivity of 8.1−9.5 Ω cm) with dimensions of 1.5 × 1 cm^2 was cleaned with distilled water and absolute ethanol in an ultrasound bath for 15 min, respectively. The silicon wafer covered the quartz boat, and the vertical distance between the Zn source and the Si substrate was approximately 9 mm. The boat was placed at the center of the chamber resistance furnace, and heated at a rate of 10 °C min^{-1} to 450 °C and kept for 30 min. Then, the furnace was switched off and was cooled to room temperature naturally. Finally, gray products were deposited on the silicon substrate. **ZnO hexagonal nanodisk networks:** 0.040 g of $ZnCl_2$ powders were mixed with 0.010 g of $InCl_3{\cdot}4H_2O$ to form a mixture. The mixture was used instead of 0.040 g of $ZnCl_2$ powders. The gray products were obtained via the same experimental procedure.

The as-prepared products were characterized and analyzed by X-ray diffraction (XRD), scanning electron microscopy (SEM), and transmission electron microscopy (TEM). The XRD analysis was performed using a Rigaku DMX-IIIC X-ray diffractometer with Cu $K\alpha_1$ radiation (λ = 1.54 A) at 40 kV and 30 mA. SEM images were obtained on a FEI Quanta 200 scanning electron microscope at an accelerating voltage of 20 kV. The chemical compositions were measured by an energy-dispersive X-ray spectroscopy (EDS) system attached to the SEM. TEM images were obtained on a JEOL JEM-3010 transmission electron microscope at an accelerating voltage of 300 kV. Samples for TEM were prepared by dispersing the ZnO samples on a carbon-coated copper grid. Photoluminescence (PL) spectra were measured at room temperature on a Hitachi F-4600 fluorescence spectrophotometer using a Xe lamp with an excitation wavelength of 300 nm.

3. RESULTS AND DISCUSSION

3.1. Structural Characterization. The products synthesized by heating $ZnCl_2$ and mixture of $ZnCl_2$ and $InCl_3{\cdot}4H_2O$ at 450 °C for 30 min were characterized by SEM and XRD, the results are shown in Figures 2 and 3. Figure 2a shows top-view SEM images of the products obtained via heating 0.040 g $ZnCl_2$. It can be seen that a large-scale array of ordered nanorods cover on the Si substrate. The ZnO nanorods have flate hexagonal crystallographic planes (the inset of Figure 2a), indicating partially that the ZnO nanorods are hexagonal in

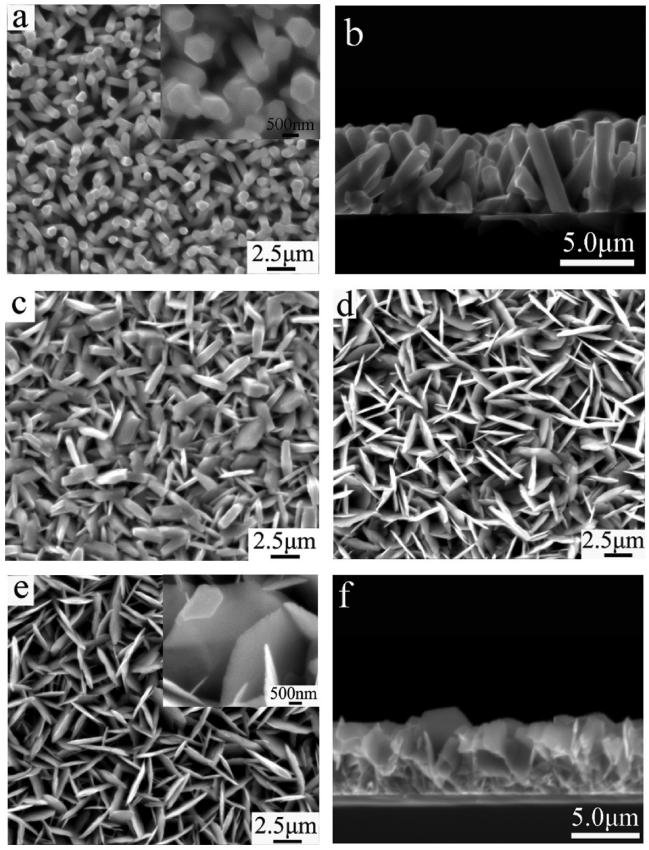

Figure 2. SEM images of the products synthesized by heating $ZnCl_2$ and a mixture of $ZnCl_2$ and $InCl_3{\cdot}4H_2O$ at 450 °C for 30 min. (a) Top-view SEM images of the products obtained via heating 0.040 g of $ZnCl_2$, (b) Cross-sectional SEM image of the nanorod arrays, (c−e) Top-view SEM images of the products obtained via heating mixtures of 0.0025 g (c), 0.005 g (d), or 0.010 g (e) of $InCl_3{\cdot}4H_2O$ and 0.040 g of $ZnCl_2$. (f) Cross-sectional SEM image of the nanodisk network obtained by adding 0.010 g of $InCl_3{\cdot}4H_2O$ into 0.040 g of $ZnCl_2$.

crystal structure and preferentially oriented in the *c*-axis direction. The diameters of nanorods are in the range of 0.64 to 0.91 μm. Figure 2b shows the cross-sectional SEM image of the nanorod arrays. The nanorods are oriented vertically with respect to the Si substrate, and have length of about 5.1 μm. When 0.0025 g $InCl_3{\cdot}4H_2O$ was added into 0.040 g $ZnCl_2$, the as-obtained products are composed of a large quantity of thick sheet like structures instead of nanorod arrays (Figure 2c). The nanosheets have widths in the range of 2.0−2.7 μm and thicknesses of 0.33−0.98 μm. When weight of $InCl_3{\cdot}4H_2O$ is increased to 0.005 and 0.010 g, respectively, the products consist of a large quantity of hexagonal nanodisks. These nanodisks intercross with each other to form a network structure (Figure 2d−f). The widths of the nanodisks are in the range of 2.4−3.4 μm and 2.5−3.7 μm, respectively. Thicknesses are decreased to the range of 0.19−0.41 μm and 0.15−0.32 μm, respectively. Figure 2f shows the cross-sectional SEM image of the nanodisk networks obtained by adding 0.010 g of $InCl_3{\cdot}4H_2O$. The nanodisks are oriented vertically with respect to the Si substrate, and have length of about 5.0 μm. The XRD patterns of the as-prepared nanostructures with different morphologies are shown in Figure 3. Figure 3a exhibits the XRD pattern of nanorod arrays obtain by heating $ZnCl_2$. All diffraction peaks can be attributed to the wurtzite ZnO with the hexagonal structure, which are in a good agreement with Joint

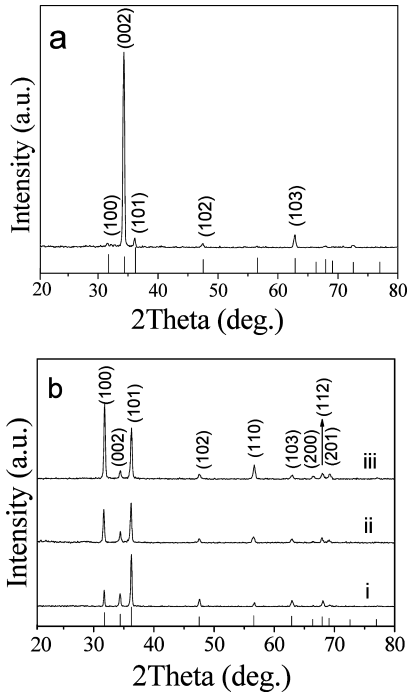

Figure 3. (a) XRD pattern of nanorod arrays obtain by heating 0.040 g of $ZnCl_2$, (b) XRD patterns of sheet like structures obtained by heating mixtures of 0.0025 g (i), 0.005 g (ii), or 0.010 g (iii) of $InCl_3{\cdot}4H_2O$ and 0.040 g of $ZnCl_2$.

Committee on Powder Diffraction Standards (JCPDS) card No. 36-1451. Furthermore, the relative intensities of these peaks are distinct from those of ZnO powders. The (002) diffraction peak is overwhelming, and other peaks are very weak, revealing a preferred orientation of the nanorods along their *c*-axis. The degree of the orientation can be illustrated by the relative texture coefficient,[48] which is given by

$$TC_{002} = \frac{I_{002}/I^0_{002}}{I_{002}/I^0_{002} + I_{101}/I^0_{101}} \quad (1)$$

where TC_{002} is the relative texture coefficient of diffraction peaks (002) over (101), I_{002} and I_{101} are the measured diffraction intensities due to (002) and (101) planes, respectively. I^0_{002} and I^0_{101} are the corresponding values of standard PDF measured from randomly oriented powder samples. For materials with random crystallographic orientations, for example, powders, the texture coefficient is 0.5. The value of our sample is 0.972, which indicates an extremely high c-orientation of the ZnO nanorods. The XRD patterns of the as-prepared ZnO nanodisks obtained by heating the mixture of $InCl_3{\cdot}4H_2O$ and $ZnCl_2$ are shown in Figure 3b. All diffraction peaks can be assigned to ZnO with the hexagonal structures and no other peaks were observed, which reveal that the as-prepared nanodisks are pure hexagonal ZnO phases.

Moreover, the diffraction intensity of the (100) increases with increasing weight of $InCl_3{\cdot}4H_2O$, which indicates the *a*-oriented nature of the as grown hexagonal phase ZnO nanodisks. The degree of the orientation can be illustrated by the relative texture coefficient, which is given by

$$TC_{100} = \frac{I_{100}/I^0_{100}}{I_{100}/I^0_{100} + I_{101}/I^0_{101}} \quad (2)$$

where TC_{100} is the relative texture coefficient of diffraction peaks (100) over (101), I_{100} and I_{101} are the measured diffraction intensities due to (100) and (101) planes, respectively. I^0_{100} and I^0_{101} are the corresponding values of standard PDF measured from randomly oriented powder samples. When the weight of $InCl_3{\cdot}H_2O$ is 0.005 and 0.010 g, the TC_{100} of ZnO nanodisks is 0.598 and 0.733, respectively. The results reveal the products obtained by adding 0.005 and 0.010 g of $InCl_3{\cdot}4H_2O$ are ZnO nanodisk networks with preferable *a*-orientation.

Further morphological and structural characterization of the ZnO nanorods and nanodisks was investigated by TEM, and the results are shown in Figures 4 and 5. Figure 4a shows a

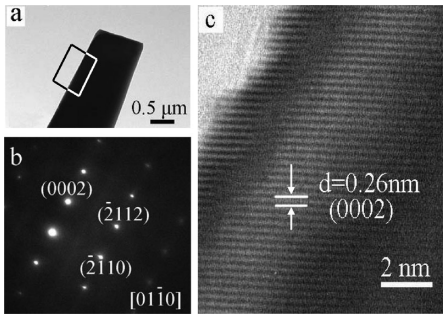

Figure 4. (a) TEM image of a single nanorod, (b) SEAD pattern, and (c) HRTEM image from box in a.

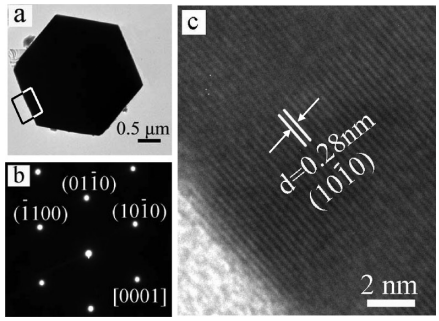

Figure 5. (a) TEM image of a single hexagonal nanodisk, (b) SEAD pattern and (c) HRTEM image from box in a.

typical TEM image of a single ZnO nanorod. The diameter of the ZnO nanorod is 0.81 μm, which is in good agreement with the SEM results. The selected-area electron diffraction (SAED) pattern from box in panel a is shown in the Figure.4b, which can be indexed as the [01$\bar{1}$0] zone axis of single-crystalline ZnO with the hexagonal structures. The high resolution TEM (HRTEM) image shown in Figure 4c gives a lattice fringe spacing of 0.26 nm, corresponding to the *d* spacing of (0002) crystal planes of hexagonal phase. Both the SAED and the HRTEM confirm that the ZnO nanorods are single crystalline and grow along the [001] direction, which is consistent with the XRD result. The TEM and HRTEM images and SAED pattern of the ZnO nanodisks are shown in Figure 5. Figure 5a shows a typical TEM image of a single ZnO nanodisk. The nanodisk has perfect hexagonal shape with a uniform side length of 1.5 μm and diagonal of 2.7 μm. The SAED pattern shown in Figure 5b can be indexed as the [0001] zone axis of single-crystalline ZnO with a hexagonal structure. The HRTEM image is displayed in Figure 5c. The *d* spacing of 0.28 nm between adjacent lattice planes corresponds to the distance

between two $(10\bar{1}0)$ crystal plans. The SAED and HRTEM results indicate that the nanodisk grew mainly along the six symmetric directions perpendicular to $(10\bar{1}0)$, $(\bar{1}010)$, $(01\bar{1}0)$, $(0\bar{1}10)$, $(\bar{1}100)$, and $(1\bar{1}00)$ facets, and are enclosed by ± (0001) top and bottom surfaces.

3.2. Growth Mechanism. To better understand the growth mechanism of ZnO nanorod arrays and nanodisk networks, time-dependent experiments were carried out, the resultant products were analyzed by SEM and XRD, and the results are shown in Figure 6–9. Figure 6a shows SEM image of the products (sample 1) obtained by heating $ZnCl_2$ to 450 °C and stopping immediately. The SEM observation indicates that the products are dense films constructed from ZnO micrometer sized particles with the sizes of 2.9 to 3.9 μm, and some particles have flate hexagonal crystallographic planes. SEM image of the products (sample 2) obtained by heating $ZnCl_2$ at 450 °C for 10 min is shown in Figure 6b, which indicates that ZnO particle sizes are increased to the range of 4.0–4.8 μm, and most ZnO particles have flate hexagonal crystallographic planes. When the heat treatment time is prolonged to 20 min,

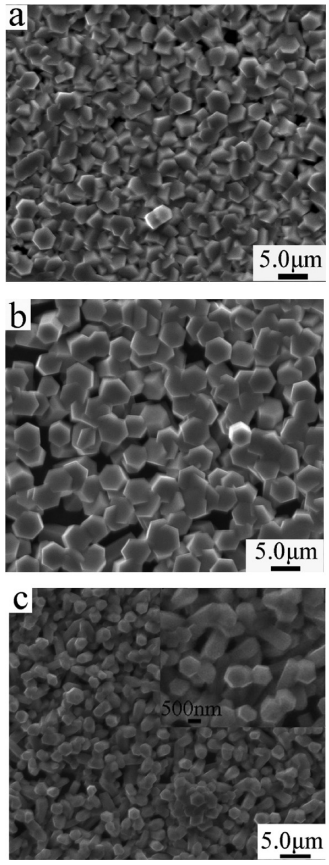

Figure 6. (a) SEM image of the products (sample 1) obtained by heating $ZnCl_2$ to 450 °C and stopping immediately. (b–c) SEM images of the products (samples 2 and 3) obtained by heating $ZnCl_2$ at 450 °C for (b) 10 and (c) 20 min, respectively.

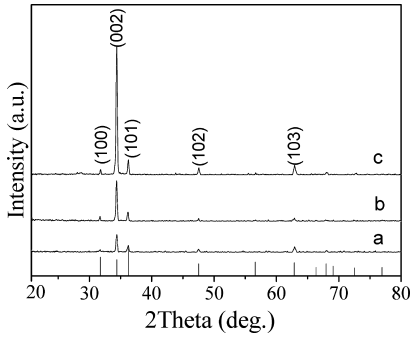

Figure 7. (a) XRD pattern of the products (sample 1) obtained by heating $ZnCl_2$ to 450 °C and stopping immediately. (b–c) XRD patterns of the products (samples 2 and 3) obtained by heating $ZnCl_2$ at 450 °C for (b) 10 and (c) 20 min, respectively.

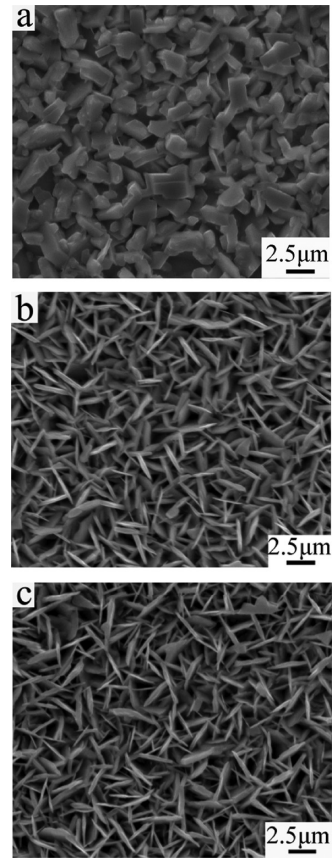

Figure 8. (a) SEM images of the products (sample 4) synthesized by heating mixtures of 0.010 g $InCl_3{\cdot}4H_2O$ and 0.040 g $ZnCl_2$ to 450 °C and stopping immediately; (b–c) SEM images of the products (samples 5 and 6) obtained by heating the mixtures of $InCl_3{\cdot}4H_2O$ and $ZnCl_2$ at 450 °C for (b) 10 and (c) 20 min, respectively.

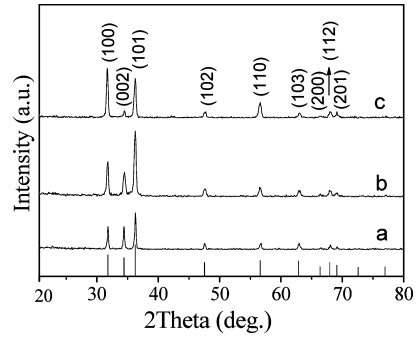

Figure 9. XRD pattern of the products (sample 4) synthesized by heating the mixtures of $InCl_3{\cdot}4H_2O$ and $ZnCl_2$ to 450 °C and stopping immediately; (b–c) XRD patterns of the products (samples 5 and 6) obtained by heating the mixtures of $InCl_3{\cdot}4H_2O$ and $ZnCl_2$ at 450 °C for (b) 10 and (c) 20 min, respectively.

ZnO nanorods with the diameters of 0.61 to 0.89 μm grow out on the ZnO nanoparticle film (Figure 6c, sample 3). The corresponding XRD patterns are shown in Figure 7, which reveal that the as-prepared ZnO nanoparticle film and nanorod arrays are ZnO with the hexagonal structures. Moreover, relative to the other peaks, the (002) diffraction peak is overwhelming, which indicates that the as-prepared ZnO nanoparticle film and nanorod arrays preferentially oriented in the [001] direction. TC_{002}, the relative texture coefficient of diffraction peaks (002) over (101) of samples 1, 2, and 3 calculated by eq 1 is 0.851, 0.897, and 0.945, respectively. Figure 8a shows SEM image of the products (sample 4) obtained by heating the mixture of 0.010 g $InCl_3{\cdot}4H_2O$ and 0.04 g $ZnCl_2$ to 450 °C and stopping immediately. The products are dense films constructed from ZnO thick nanosheets with the widths of 2.2−2.6 μm and thicknesses of 0.73−2.1 μm. When the heat treatment time is prolonged to 10 and 20 min, respectively, the products (Figures.8b and c, samples 5 and 6) are the nanodisk networks constructed from ZnO hexagonal nanodisk. The widths of samples 5 and 6 are 2.3−2.9 μm and 2.5−3.3 μm, and their thicknesses are 0.26 to 0.41 μm and 0.25 to 0.34 μm, respectively. The corresponding XRD patterns are shown in Figure 9, which reveal that the as-prepared ZnO nanosheet films and nanodisk networks are ZnO with the hexagonal structures. In addition, the diffraction intensity of the (100) increases with heat treatment time, indicating the nanodisk networks preferentially oriented in the [100] direction. TC_{100}, the relative texture coefficient of diffraction peaks (100) over (101) of samples 5, and 6 calculated by eq 2 is 0.531 and 0.693, respectively. In addition, an isolated ZnO nanodisk was found on the nanodisk networks obtained by heating the mixture of 0.005 g $InCl_3{\cdot}4H_2O$ and 0.04 g $ZnCl_2$ at 450 °C for 0.5 h as shown in Figure 10a. EDS spectra from boxes 1and 2 in (a) are shown in Figures.10b and c, respectively. These EDS spectra indicate that the nanodisk consists of O, Zn, In and Cl elements, and the weight and atomic ratios of the elements are given in table 1. From this table, it is observed that the content of indium in box 1 is higher than that in box 2. These results suggest that the doped In ions are accumulated in the *c* planes of ZnO.

Until now there have been two well-accepted mechanisms for the growth of one-dimensional nanostructure, the vapor−liquid−solid (VLS) and the vapor−solid (VS) mechanisms. In this study, no liquid droplet was found at the end of the nanorods, and thus the growth of the ZnO nanorods may be governed by VS process. The $ZnCl_2$ powder was vaporized to form $ZnCl_2$ vapor during the heat treatment. The $ZnCl_2$ vapor reacted with residual H_2O vapor in the reaction chamber to form ZnO vapor. The specific chemical reactions can be formulated as follows:

$$ZnCl_2(s) \rightarrow ZnCl_2(g) \quad (3)$$

$$ZnCl_2(g) + H_2O(g) = ZnO(g) + 2HCl(g) \quad (4)$$

On the basis of the investigations described above, a possible mechanism to form ZnO nanorod arrays was proposed. As illustrated in Figure 11, When the $ZnCl_2$ is heated to 450 °C, the ZnO vapor formed by reaction 4 deposited directly on the surface of the Si substrate to form crystalline nuclei via the VS process, and thus ZnO nanoparticle films are obtained (Figure 11b). When the heat treatment time is prolonged to 10 min, the ZnO nanoparticles are grown into nanoparticles with the bigger sizes to form ZnO nanoparticle films oriented in the

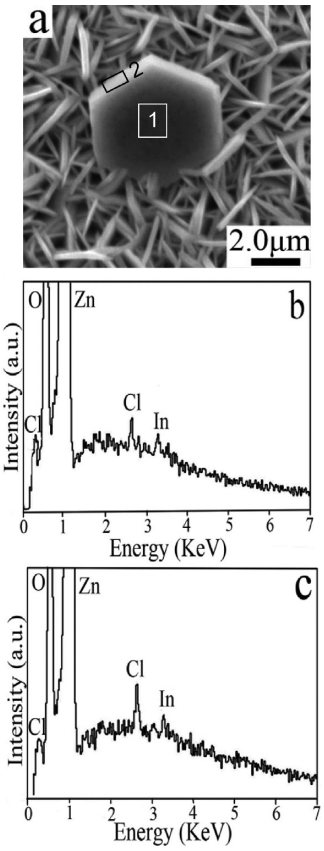

Figure 10. (a) SEM image of an isolated ZnO nanodisk on the nanodisk networks obtained by heating the mixture of 0.005 g $InCl_3{\cdot}4H_2O$ and 0.04 g $ZnCl_2$ at 450 °C for 0.5 h. (b−c) EDS spectra from boxes 1and 2 in a, respectively.

[001] direction (Figure 11c). The oriented ZnO nanoparticle films served as seeds for subsequent growth of highly oriented ZnO nanorods. As we know, ZnO is a polar crystal with the hexagonal structure, and consists of a positive polar (0001) plane rich in Zn cations, a negative polar $(000\bar{1})$ plane rich in O anions, and a nonpolar $\{01\bar{1}0\}$ plane. The surface energy of {0001} facets is generally higher than that of $\{01\bar{1}0\}$ facets.[1] Thus, when the heat treatment time is increased to 20 min, the nanorods grow out on the oriented ZnO nanoparticle film along the *c*-axis (Figure 11d). Finally, ZnO nanorod arrays preferentially oriented in the [001] direction are formed (Figure 11e). When $InCl_3{\cdot}4H_2O$ was introduced into the reaction system, the as-obtained products are ZnO nanodisk networks preferentially oriented in the [100] direction instead of nanorod arrays preferentially oriented in the [001] direction. It is reasonable to conclude that $InCl_3{\cdot}4H_2O$ plays an important role in the ZnO microstructural evolution. In the reaction chamber for growth of nanodisk networks, in addition to reactions 3 and 4, $InCl_3{\cdot}4H_2O$ powders were decomposed to $InCl_3$ vapor and H_2O vapor (reaction 5). As ZnO nanocrystals were formed via reaction 4, $InCl_3$ vapor reacted with H_2O vapor in the reaction chamber to form In_2O_3 vapor (reaction 6). In^{3+} ions were adulterated at the crystal lattice of ZnO nanocrystals. The doped In^{3+} ions are accumulated in the *c* planes of ZnO to form defects, which reduced the surface energy of ZnO (0001) leading to the fastest growth of ZnO nanocrystals along $\langle 01\bar{1}0\rangle$,[47] and thus the hexagonal nanodisks are obtained.

Table 1. Chemical Compositions of Different Regions of the Isolated ZnO Nanodisk

	O		Zn		Cl		In	
	wt %	at %	wt %	at %	wt %	at %	wt %	at %
region 1	12.47	36.85	85.63	61.93	0.48	0.64	1.42	0.59
region 2	10.40	32.15	88.01	66.59	0.60	0.83	0.99	0.43

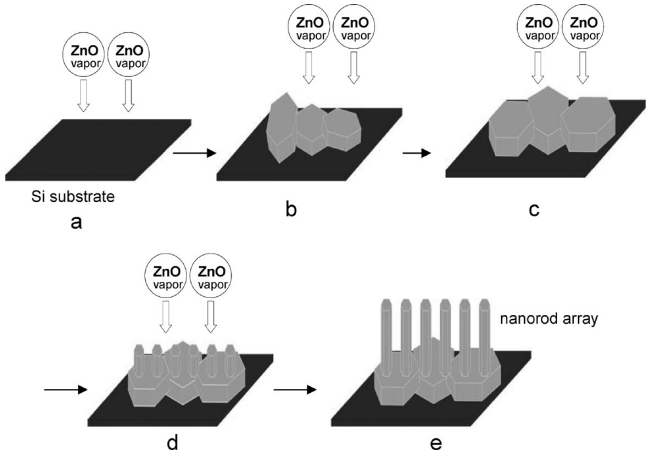

Figure 11. Schematic diagram of the growth mechanism of the ZnO nanorod arrays.

$$InCl_3 \cdot 4H_2O(s) = InCl_3(g) + 4H_2O(g) \quad (5)$$

$$2InCl_3(g) + 3H_2O(g) = In_2O_3(g) + 6HCl(g) \quad (6)$$

On the basis of the aforementioned experimental results and our analysis, the growth of the ZnO nanodisks may be governed by VS process, and a possible mechanism was proposed. As illustrated in Figure 12. When the mixture of

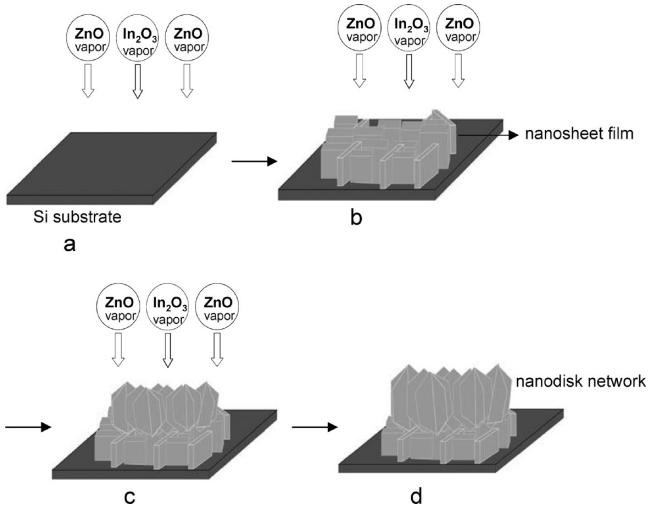

Figure 12. Schematic diagram of the growth mechanism of the ZnO nanodisk networks.

$ZnCl_2$ and $InCl_3 \cdot 4H_2O$ is heated to 450 °C, the ZnO vapor formed by reaction 4 deposited directly on the Si substrate to form ZnO crystalline nuclei via the VS process. The ZnO crystalline nuclei grew into thick nanosheets due to the local segregation of the doping element of indium, as a result, ZnO thick nanosheet films are obtained (Figure 12b). The ZnO thick nanosheet films served as seeds for subsequent growth of highly oriented ZnO nanodisk networks. When the heat treatment time is prolonged to 10 min, the hexagonal nanodisks grow out on the nanosheet films along $\langle 01\bar{1}0 \rangle$ directions, to form ZnO nanodisk networks (Figure 12c). The hexagonal nanodisk sizes increase with an increase on the heat treatment time (Figure 12d).

3. 3. Photoluminescence. Photoluminescence (PL) spectra of ZnO nanorod arrays and nanodisk networks were measured at room temperature using a Xe lamp with an excitation wavelength of 300 nm, the results are shown in Figure 13. A UV emission peak at 379 nm and a very weak blue

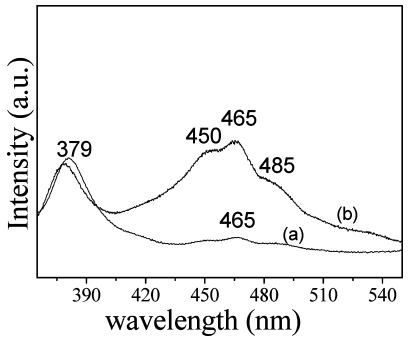

Figure 13. PL spectra of the as-synthesized (a) nanorod arrays and (b) nanodisk networks.

green emission peak at 465 nm were observed in the PL spectrum for ZnO nanorod arrays. However, in addition to UV emission peak, three strong blue green emission peaks at 450, 465, and 485 nm were observed in the PL spectrum for ZnO nanodisk networks. The UV peak is attributed to a near band-edge emission, namely the recombination of free excitons between conductive band and valence band.[49] The blue-green emission mainly originates from defect states such as Zn interstitials and oxygen vacancies. The 450 nm emission corresponds to the electron transition from the shallow donor level of oxygen vacancy and zinc interstitials to the valence band.[50] The emission at 465 nm may be in correlation with the defect structures.[51] The emission at 485 nm corresponds to the transition between the oxygen vacancy and interstitial oxygen.[52] The tervalent indium cations can combine more oxygen atoms than bivalent zinc cations, because of the different coordinate linkage number. Therefore, there are more oxygen related defects In-doped ZnO than that of undoped ZnO,[53] and thus strong blue-green emissions were observed in ZnO nanodisk networks.

3.4. Field Emission Behaviors. Nanodisk networks and nanorod arrays are ideal objects for electron field emission. The FE measurements of the as-grown ZnO nanorod arrays and nanodisk networks were carried out in a vacuum chamber. The as-prepared ZnO nanostructures on the silicon substrate with an area of 25 mm^2 were used as a cathode, the indium-doped tin oxide (ITO) glass plate as an anode. The distance between the anode and the cathode is fixed at about 210 μm, and the schematic diagram of the FE measurement system is shown in Figure 14a. The vacuum was kept at about 1.0×10^{-4} Pa during

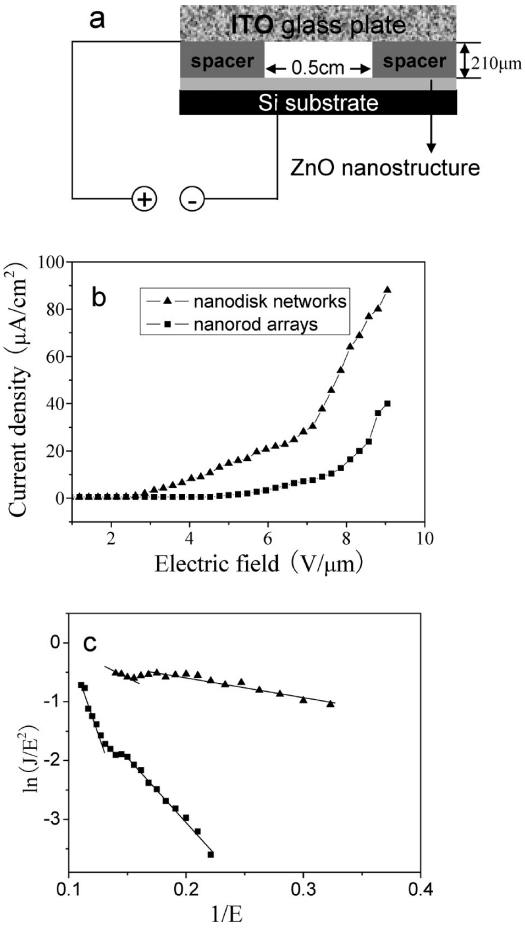

Figure 14. (a) Schematic illustration of the FE measurement system. (b) FE current density vs electric field (J–E) for ZnO nanorod arrays and nanodisk networks. (c) The corresponding F–N plots of ZnO nanorod arrays and nanodisk networks.

measurements. The applied voltage was increased from 0 to 1900 V with a step of 50 V. Figure 14b shows the FE current density-the field intensity data from the ZnO nanorod arrays and nanodisk networks. The turn-on electric field (the electric field required to produce an emission current density of 1 μA cm^{-2}) for the ZnO nanorod arrays and nanodisk networks is 4.8 and 2.6 V μm^{-1}, respectively. The value of turn-on field for the ZnO nanodisk networks is lower than the data from the nanorod arrays,[35,37] nanowire arrays,[38] nanoneedles,[42] nanotetrapods[40] and triangle-like nanosheets[44] of ZnO. On the basis of the Folwer–Nordheim (F–N) model,[34] FE current from a metal or semiconductor is attributed to the tunneling of electrons from the material into a vacuum through a potential barrier under the influence of an electric field, and the relationship between the current density (J) and the field strength (E) can be depicted as

$$J = \frac{A\beta^2E^2}{\phi}\exp\left(-\frac{B\phi^{3/2}}{\beta E}\right) \quad (7)$$

where ϕ is the work function of the emitter, which is 5.3 eV for ZnO,[34] β is the field-enhancement factor, which is related to the emitter geometry, crystal structure, and spatial distribution of the emitting centers, A and B are constants with values of 1.5 $\times$ 10^{-10} (A eV V^{-2}) and 6.83 $\times$ 10^3 eV$^{-3/2}$ μm^{-1}, respectively. Figures 14c shows the F–N plot of the J–E curves, that is, ln (J/E$^{2)}$ versus 1/E, for ZnO nanorod arrays and nanodisk networks. From this figure, it is observed that the F–N plot of ZnO nanostructures exhibits a two slope behavior. This type of nonlinearity in the F–N plot has been reported by Yuvaraj et al.[54] Ramgir et al.[55] and Premkumar.[56]The two-slope behavior was explained on the basis of the electron emission from the conduction band (CB) and valence bands (VB). The electron emission occurs from the CB (ϕ = 5.3 eV) in the lower field. When the applied field is increased further, the electrons in the VB, that is, 3.37 eV below the CB, contribute to the emission current together with the electrons from the CB. Now, the effective work function is $\phi_0 = \phi + Eg$ = 5.3 + 3.37 = 8.67 eV. The field enhancement factor, β, is calculated from the slopeof the F–N plot. In this work, different slope ($-B\phi^{3/2}/\beta$) values were observed in the lower and high field. The β value for the ZnO nanorod arrays and nanodisk networks were calculated using ϕ = 5.3 eV in the lower field and ϕ_0 = 8.67 eV in the higher field. The results have been listed in Table 2. The β value of the nanodisk networks is greater than that of nanorod arrays,[35,36] nanoneedles,[42] nanowire arrays,[39] hierarchical nanostructures,[43] nanotetrapods,[40] nanocone arrays[41] and triangle-like nanosheets[44] of ZnO. These comparative results indicate that the as-synthesized ZnO hexagonal nanodisk networks possess excellent FE performance, and are a promising candidate in future FE device applications. The excellent FE performance is attributed to the small radius of curvature for hexagonal emitter and the well vertical align on the substrates.[34,45] Moreover, it can effectively improve the FE property to dope indium in ZnO nanodisks because of the carrier concentration increasing, which results in the increase of the field enhancement factor and the reduction of the work function.[45,57]

Table 2. Field Enhancement Factor (β) Calculated for Different Structures of ZnO

	field enhancement factor (β)	
	lower field (ϕ = 5.3 eV)	higher field (ϕ = 8.67 eV)
ZnO nanorod arrays	2798	2234
ZnO nanodisk networks	12499	9264

4. CONCLUSIONS

In summary, ZnO nanorod arrays and hexagonal nanodisk networks were synthesized via a very simple low temperature chemical vapor deposition process. Their controlled synthesis is achieved by varying chemical composition of the Zn source. The function of $InCl_3{\cdot}4H_2O$ in evolution of the both nanostructures has been studied, and possible mechanisms are proposed to account for the growth of the ZnO nanorod arrays and hexagonal nanodisk networks. This simple and mild approach to fabricate ZnO hexagonal nanodisk networks can be easily scaled up, and potentially extended to the synthesis of other semiconductor nanodisk networks. The FE properties of the ZnO nanorod arrays and nanodisk networks were investigated. The results indicate that ZnO hexagonal nanodisk networks exhibit enhanced FE properties and are promising candidate in future field-emission-based device applications.

AUTHOR INFORMATION

Corresponding Author

*Fax: 0086-29-81530702. E-mail: hqyang@snnu.edu.cn.

Notes

The authors declare no competing financial interest.

■ ACKNOWLEDGMENTS

This work was supported by the National Natural Science Foundation of China (Grant No. 21073116), the Natural Science Foundation of Shanxi Province (Grant No.2010JM2011) and the Fundamental Research Funds for the Central Universities (Grant No. GK201101004).

■ REFERENCES

(1) Wang, Z. L. *J. Phys.:Condens. Matter* **2004**, *16*, R829−R858.
(2) Aleksandra, B. D.; Leung, Y. H. *Small* **2006**, *2* (8- 9), 944−961.
(3) Pan, Z. W.; Dai, Z. R.; Wang, Z. L. *Science* **2001**, *291*, 1947−1949.
(4) Wang, X. D.; Christopher, J. S.; Wang, Z. L. *Nano Lett.* **2004**, *4* (3), 423−426.
(5) Sun, Y.; Fuge, G. M.; Fox, N. A.; Riley, D. J.; Ashfold, M. N. R. *Adv. Mater.* **2005**, *17*, 2477−2481.
(6) Park, W. I.; Yi, G. C.; Kim, M. Y.; Pennycook, S. J. *Adv. Mater.* **2002**, *14* (24), 1841−1483.
(7) Lao, J. Y.; Huang, J. Y.; Wang, D. Z.; Ren, Z. F. *Nano Lett.* **2003**, *3* (2), 235−238.
(8) Kong, X. Y.; Ding, Y.; Yang, R. S.; Wang, Z. L. *Science* **2004**, *303*, 1348−1351.
(9) Hughes, W. L.; Wang, Z. L. *J. Am. Chem. Soc.* **2004**, *126*, 6703−6709.
(10) Gao, P. X.; Wang, Z. L. *Small* **2005**, *1* (10), 945−949.
(11) Gao, P. X.; Ding, Y.; Mai, W. J.; Hughes, W. L.; Lao, C. S; Wang, Z. L. *Science* **2005**, *309*, 1700−1704.
(12) Xu, C. X.; Sun, X. W.; Dong, Z. L.; Yu, M. B. *Appl. Phys. Lett.* **2004**, *85* (17), 3878−3880.
(13) Lao, C. S.; Gao, P. X.; Yang, R. S.; Zhang, Y.; Dai, Y.; Wang, Z. L. *Chem. Phys. Lett.* **2005**, *417*, 359−363.
(14) Gao, P. X.; Wang, Z. L. *J. Am. Chem. Soc.* **2003**, *125*, 11299−11305.
(15) Yu, W. D.; Li, X. M.; Gao, X. D. *Cryst. Growth Des.* **2005**, *5* (1), 151−155.
(16) Joo, J.; Kwon, S. G.; Yu, J. H.; Hyeon, T. *Adv. Mater.* **2005**, *17*, 1873−1877.
(17) Umar, A.; Lee, S.; Lee, Y. S.; Nahm, K. S.; Hahn, Y. B. *J. Cryst. Growth* **2005**, *277*, 479−484.
(18) Lao, J. Y.; Wen, J. G.; Ren, Z. F. *Nano Lett.* **2002**, *2* (11), 1287−1291.
(19) Gao, P. X.; Lao, C. S.; Hughes, W. L.; Wang, Z. L. *Chem. Phys. Lett.* **2005**, *408*, 174−178.
(20) Kim, D. S.; Ji, R.; Fan, H. J.; Bertram, F.; Scholz, R.; Dadgar, A.; Nielsch, K.; Krost, A.; Christen, J.; Gösele, U.; Zacharias, M. *Small* **2007**, *3* (1), 76−80.
(21) Tsao, F. C.; Chen, J. Y.; Kuo, C. H.; Chi, G. C.; Pan, C. J.; Huang, P. J.; Tun, C. J.; Pong, B. J.; Hsueh, T. H.; Chang, C. Y.; Pearton, S. J.; Ren, F. *Appl. Phys. Lett.* **2008**, *92*, 203110.
(22) Gao, P. X.; Wang, Z. L. *Appl. Phys. Lett.* **2004**, *84* (15), 2883−2885.
(23) Lai, E.; Kim, W.; Yang, P. D. *Nano Res.* **2008**, *1*, 123−128.
(24) Huang, M. H.; Mao, S.; Feick, H. N.; Yan, H. Q.; Wu, Y. Y.; Kind, H.; Weber, E.; Russo, R.; Yang, P. D. *Science* **2001**, *292*, 1897−1899.
(25) Law, M.; Greene, L.; Johnson, J. C.; Saykally, R.; Yang, P. D. *Nat. Mater.* **2005**, *4*, 455−459.
(26) Ko, S. H.; Lee, D.; Kang, H. W.; Nam, K. H.; Yeo, J. Y.; Hong, S. J.; Grigoropoulos, C. P.; Sung, H. J. *Nano Lett.* **2011**, *11*, 666−671.
(27) Fei, P.; Yeh, P. H.; Zhou, J.; Xu, S.; Gao, Y. F.; Song, J. H.; Gu, Y. D.; Huang, Y. Y.; Wang, Z. L. *Nano Lett.* **2009**, *9* (10), 3435−3439.
(28) Wang, Z. L.; Song, J. H. *Science* **2006**, *312*, 241−246.
(29) Hu, Y. F.; Zhang, Y.; Xu, C.; Zhu, G.; Wang, Z. L. *Nano Lett.* **2010**, *10*, 5025−5031.
(30) Hsueh, T. J.; Hsu, C. L.; Chang, S. J.; Chen, I. C. *Sens. Actuators B* **2007**, *126*, 473−477.
(31) Wan, Q.; Li, Q. H.; Chen, Y. J.; Wang, T. H.; He, X. L.; Li, J. P.; Lin, C. L. *Appl. Phys. Lett.* **2004**, *84* (18), 3654−3656.
(32) Park, W. I.; Kim, J. S.; Yi, G. C.; Lee, H. J. *Adv. Mater.* **2005**, *17*, 1393−1397.
(33) Saito, Y.; Uemura, S. *Carbon* **2000**, *38*, 169−182.
(34) Fang, X. S.; Bando, Y. S.; Gautam, U. K.; Ye, C. H.; Golberg, D. *J. Mater. Chem.* **2008**, *18*, 509−522.
(35) Liu, J. P.; Xu, C. X.; Zhu, G. P.; Li, X.; Cui, Y. P.; Yang, Y.; Sun, X. W. *J. Phys. D: Appl. Phys.* **2007**, *40*, 1906−1909.
(36) Umar, A.; Kim, S. H.; Lee, H. S.; Lee, N.; Hahn, Y. B. *J. Phys. D: Appl. Phys.* **2008**, *41*, 065412.
(37) Zhang, Y.; Lee, C. T. *J. Phys. Chem. C* **2009**, *113*, 5920−5923.
(38) Lee, C. J.; Lee, T. J.; Lyu, S. C.; Zhang, Y.; Ruh, H.; Lee, H. J. *Appl. Phys. Lett.* **2002**, *81*, 3648−3650.
(39) Chen, C. H.; Chang, S. J.; Chang, S. P.; Tsai, Y. C.; Chen, I. C.; Hsueh, T. J.; Hsu, C. L. *Chem. Phys. Lett.* **2010**, *490*, 176−179.
(40) Huang, Y.; Yu, K.; Cui, Q. Y.; Wang, C. C.; Zhang, N.; Zhu, Z. Q. *Mater. Lett.* **2008**, *62*, 1342−1344.
(41) Ye, C. H.; Bando, Y.; Fang, X. S.; Shen, G. Z.; Golberg, D. *J. Phys. Chem. C* **2007**, *111*, 12673−12676.
(42) Maiti, U. N.; Ahmed, S. F.; Mitra, M. K.; Chattopadhyay, K. K. *Mater. Res. Bull.* **2009**, *44*, 134−139.
(43) Wang, Z. Q.; Gong, J. F.; Su, Y.; Jiang, Y. W.; Yang, S. G. *Cryst. Growth Des.* **2010**, *10*, 2455−2459.
(44) Li, L. J.; Yu, K.; Peng, D. Y.; Zhang, Z.; Zhu, Z. Q. *Appl. Surf. Sci.* **2009**, *256*, 208−212.
(45) Pradhan, D.; Kumar, M.; Ando, Y.; Leung, K. T. *J. Phys. Chem. C.* **2008**, *112*, 7093−7096.
(46) Zhang, Z. S.; Huang, J. Y.; He, H. P.; Lin, S. S.; Tang, H. P.; Lu, H. M.; Ye, Z. Z. *Solid-State Electron.* **2009**, *53*, 578−583.
(47) Qi, J. J.; Zhang, Y.; Huang, Y. H.; Liao, Q. L.; Liu, J. *Appl. Phys. Lett.* **2006**, *89*, 252115.
(48) Yang, H. Q.; Song, Y. Z.; Li, L.; Ma, J. H.; Chen, D. C.; Mai, S. L.; Zhao, H. *Cryst. Growth Des.* **2008**, *8* (3), 1039−1043.
(49) Kong, Y. C.; Yu, D. P.; Zhang, B.; Fang, W.; Feng, S. Q. *Appl. Phys. Lett.* **2001**, *78* (4), 407−409.
(50) Zhang, D. H.; Xue, Z. Y.; Wang, Q. P. *J. Phys. D: Appl. Phys.* **2002**, *35*, 2837−2840.
(51) Shen, X. P.; Yuan, A. H.; Hu, Y. M.; Jiang, Y.; Xu, Z.; Hu, Z. *Nanotechnology* **2005**, *16*, 2039−2043.
(52) Mahamuni, S.; Borgohain, K.; Bendre, B. S.; Leppert, V. J.; Risbud, S. H. *J. Appl. Phys.* **1999**, *85* (5), 2861−2865.
(53) Zhao, J.; Yan, X.; Yang, Y.; Huang, Y.; Zhang, Y. *Mater. Lett.* **2010**, *64*, 569−572.
(54) Yuvaraj, D.; Kaushik, R.; Rao, K. N. *Appl. Mater. Interfaces* **2010**, *2*, 1019−1024.
(55) Ramgir, N.; Late, D.; Bhise, A.; Mulla, I.; More, M.; Joag, D.; Pillai, V. *Nanotechnology* **2006**, *17*, 2730−2735.
(56) Premkumar, T.; Zhou, Y. S.; Lu, Y. F.; Baskar, K. *Appl. Mater. Interfaces* **2010**, *2*, 2863−2869.
(57) Jung, M. N.; Ha, S. H.; Oh, S. J.; Koo, J. E.; Cho, Y. R.; Lee, H. C.; Lee, S. T.; Jeon, T. I.; Makino, H.; Chang, J. H. *Curr. Appl. Phys.* **2009**, *9*, e169−e172.